

Highly anisotropic quasiparticle interference patterns in the spin-density wave state of the iron pnictides

Dheeraj Kumar Singh and Pinaki Majumdar

Harish-Chandra Research Institute, Chhatnag Road, Jhansi, Allahabad 211019, India

& Homi Bhabha National Institute, Training School Complex, Anushakti Nagar, Mumbai 400085, India

(Dated: October 17, 2018)

We investigate the impurity scattering induced quasiparticle interference in the $(\pi, 0)$ spin-density wave phase of the iron pnictides. We use a five orbital tight binding model and our mean field theory in the clean limit captures key features of the Fermi surface observed in angle-resolved photoemission. We use a t-matrix formalism to incorporate the effect of doping induced impurities on this state. The impurities lead to a spatial modulation of the local density of states about the impurity site, with a periodicity of $\sim 8a_{\text{Fe-Fe}}$ along the antiferromagnetic direction. The associated momentum space quasiparticle interference pattern is anisotropic, with major peaks located at $\sim (\pm\pi/4, 0)$, consistent with spectroscopic imaging scanning tunneling microscopy. We trace the origin of this pattern to an elliptical contour of constant energy around momentum $(0,0)$, with major axis oriented along the $(0,1)$ direction, in the mean field electronic structure.

PACS numbers: 74.70.Xa, 75.10.Lp, 75.30.Fv

I. INTRODUCTION

The highly anisotropic electronic properties of the iron pnictides, with broken four-fold rotation symmetry, have been a subject of intense research in recent times. Observed in angle-resolved photoemission spectroscopy^{1,2} (ARPES), neutron magnetic resonance³ (NMR), and transport properties^{4,5}, such anisotropy is seen both in the low temperature collinear antiferromagnetic (AF) state and the high temperature, un-ordered, ‘nematic’ phase⁶.

ARPES reveal a significant energy splitting between the d_{xz} and d_{yz} orbitals below the tetragonal-to-orthorhombic transition - which may precede⁷ or coincide with⁸ the spin density wave (SDW) transition. The spin dynamics shows a strong two-fold anisotropy inside the orthorhombic domains that are formed below the structural phase transition³, optical spectra displays a significant in-plane anisotropy⁹ upto photonic energies $\sim 2\text{eV}$, and transport measurements show a larger conductivity in the antiferromagnetic direction compared to the ferromagnetic direction.

Spectroscopic imaging - scanning tunneling microscopy (SI-STM)¹⁰⁻¹⁵ provides insight into the anisotropic electronic state. Quasiparticle interference (QPI) probed by SI-STM measures the modulation of the local density of states (LDOS) induced by the impurity atoms. QPI patterns in the metallic $(\pi, 0)$ SDW state consist mainly of a quasi-one dimensional feature extended along the $q_x = 0$ line with a weaker parallel feature¹⁶⁻¹⁸ at a distance $\sim \pi/4$. Such highly anisotropic features have been attributed to impurity induced states on the anisotropic magnetic background^{19,20}.

The QPI probes the response of the ordered state to a strong localized perturbation and several attempts have been made to explain it. A reasonable description of the ARPES and QPI data imposes constraints on the electronic theory of the reference state. Broadly three frameworks have been used to model the QPI, each with some limitation.

(i) In an effective band approach²¹ LDOS modulation is strongest along the *ferromagnetic* direction while experimentally it is in the AF direction. Corresponding contours of con-

stant energy (CCE) consist mainly of a circular pocket around Γ , smaller pockets located inside, and the electron pocket around Y. (ii) A five-orbital model²² used to study QPI either produces patterns without a clear modulation²³ or shows modulation²⁴ at an energy $\omega \sim -150\text{meV}$, much larger than in the experiments. In one of the studies, details of the reconstructed FSs are not provided, while in another one large FSs consist of parallel running structures extending from Γ to the zone boundary near X ^{25,26}. (iii) First principles calculations²⁷ indicate QPI peaks at $(0, \pm\pi/4)$ and therefore the correct wavelength of modulation, $\sim 8a_{\text{Fe-Fe}}$, but again along the *ferromagnetic* direction. In this case, FSs consist of crescent like structure around Γ with the broader part facing Y. So, either the wavelength, or the orientation, or the energy of the QPI modulations remain inconsistent with experiments.

In this paper, we report on the QPI in the $(\pi, 0)$ -SDW state of an electron-doped iron pnictide. We use mean field theory on a five-orbital tight-binding model to describe the ordered state and a t-matrix calculation to quantify (single) impurity effects. We find the following: (i) Our mean field bands have several features consistent with the ARPES measurements, *e.g.*, a large elliptical pocket around Γ and adjacent four smaller pockets. (ii) The QPI is highly anisotropic, consisting of quasi-one dimensional peak structures running nearly along $q_x = \pm\pi/4$. (iii) The real-space features consist of LDOS modulation with periodicity $\sim 8a_{\text{Fe-Fe}}$ along the antiferromagnetic direction as observed in the STM measurements. The period of modulation along the AF direction is robust against change in the quasiparticle energy though the strongest modulation can shift to other direction.

II. MODEL AND METHOD

In order to study QPI in the SDW state, we consider a five-orbital tight-binding Hamiltonian defined in the Fe-As planes,

the kinetic part of which is given by

$$H_0 = \sum_{\mathbf{k}} \sum_{\mu, \nu} \sum_{\sigma} \varepsilon_{\mathbf{k}}^{\mu\nu} d_{\mathbf{k}\mu\sigma}^{\dagger} d_{\mathbf{k}\nu\sigma} \quad (1)$$

in the plane-wave basis. Here, the operator $d_{\mathbf{k}\mu\sigma}^{\dagger}$ ($d_{\mathbf{k}\mu\sigma}$) creates (destroys) an electron with spin σ and momentum \mathbf{k} in the μ -th orbital. Matrix elements $\varepsilon_{\mathbf{k}}^{\mu\nu}$, which include both the hopping matrix elements and the momentum independent on-site orbital energies, are taken from Ref.[28]. The set of d -orbitals, to which orbitals μ and ν belong, consists of d_{xz} , d_{yz} , d_{xy} , $d_{x^2-y^2}$, and $d_{3z^2-r^2}$.

The interaction part includes standard onsite Coulomb interactions

$$H_{int} = U \sum_{i, \mu} n_{i\mu\uparrow} n_{i\mu\downarrow} + (U' - \frac{J}{2}) \sum_{i, \mu < \nu} n_{i\mu} n_{i\nu} - 2J \sum_{i, \mu < \nu} \mathbf{S}_{i\mu} \cdot \mathbf{S}_{i\nu} + J \sum_{i, \mu < \nu, \sigma} d_{i\mu\sigma}^{\dagger} d_{i\mu\sigma}^{\dagger} d_{i\nu\sigma} d_{i\nu\sigma}. \quad (2)$$

U and U' are the intra-orbital and the inter-orbital Coulomb interaction, respectively. J is the Hund's coupling, with the condition $U' = U - 2J$ imposed for a rotation-invariant interaction.

The mean-field Hamiltonian for the $(\pi, 0)$ -SDW state in the two-sublattice basis is given by²⁹

$$\mathcal{H}_{mf} = \sum_{\mathbf{k}\sigma} \Psi_{\mathbf{k}\sigma}^{\dagger} (\hat{\zeta}_{\mathbf{k}\sigma} + \hat{M}_{\mathbf{k}\sigma}) \Psi_{\mathbf{k}\sigma}. \quad (3)$$

$\zeta_{\mathbf{k}\sigma}^{ll'}$ are the matrix elements due to the kinetic part while $M_{\mathbf{k}\sigma}^{ll'} = -s\sigma\Delta_{ll'}\delta^{ll'} + \frac{5J-U}{2}n_{ll'}\delta^{ll'}$. $l, l' \in s \otimes \mu$ with s and μ belonging to the sublattice and orbital bases, respectively. Off-diagonal elements of $\Delta_{ll'}$ and $n_{ll'}$ are small for the parameters considered here, and hence neglected. s and σ in front of $\Delta_{ll'}\delta^{ll'}$ take value 1 (-1) for A (B) sublattice and \uparrow -spin (\downarrow -spin), respectively. The electron field operator is defined as $\Psi_{\mathbf{k}\uparrow}^{\dagger} = (d_{A\mathbf{k}1\uparrow}^{\dagger}, d_{A\mathbf{k}2\uparrow}^{\dagger}, \dots, d_{B\mathbf{k}1\uparrow}^{\dagger}, d_{B\mathbf{k}2\uparrow}^{\dagger}, \dots)$, where subscript indices 1, 2, 3, 4, and 5 stand for orbitals $d_{3z^2-r^2}$, d_{xz} , d_{yz} , $d_{x^2-y^2}$, and d_{xy} , respectively. The exchange fields are given as $2\Delta_{ll} = U n_{ll} + J \sum_{l' \neq l} n_{ll'}$. Orbital charge density and magnetization are determined in a self-consistent manner by diagonalizing the Hamiltonian.

The change caused in the Green's function because of a single impurity with δ -potential is given by

$$\delta\hat{G}(\mathbf{k}, \mathbf{k}', \omega) = \hat{G}^0(\mathbf{k}, \omega) \hat{T}(\omega) \hat{G}^0(\mathbf{k}', \omega) \quad (4)$$

using t -matrix approximation. $\hat{G}^0(\mathbf{k}, \omega) = (\hat{\mathbf{I}} - \hat{\mathcal{H}}_{mf})^{-1}$ is the Green's function in the SDW state with

$$\hat{\mathcal{H}}_{mf}^{\prime\sigma} = \begin{pmatrix} \hat{\varepsilon}_{\mathbf{k}} & \text{sgn}\bar{\sigma}\hat{\Delta} \\ \text{sgn}\bar{\sigma}\hat{\Delta} & \hat{\varepsilon}_{\mathbf{k}+\mathbf{Q}} \end{pmatrix}. \quad (5)$$

$\hat{\mathbf{I}}$ is a 10×10 identity matrix and $\mathbf{Q} = (\pi, 0)$. $\hat{\mathcal{H}}_{mf}$ is obtained from $(\hat{\zeta}_{\mathbf{k}} + \hat{M}_{\mathbf{k}})$ using a unitary transformation³⁰ Next,

$$T(\omega) = (\hat{\mathbf{I}} - \hat{V}\hat{G}^0(\omega))^{-1}\hat{V}, \quad (6)$$

with

$$\hat{G}^0(\omega) = \frac{1}{N} \sum_{\mathbf{k}} \hat{G}^0(\mathbf{k}, \omega) \quad (7)$$

and

$$\hat{V} = V_{imp} \begin{pmatrix} \hat{\mathbf{I}} & \hat{\mathbf{I}} \\ \hat{\mathbf{I}} & \hat{\mathbf{I}} \end{pmatrix}. \quad (8)$$

Here, $\hat{\mathbf{I}}$ is a 5×5 identity matrix. The change $\delta\rho(\mathbf{q}, \omega)$ in the DOS due to the impurity scattering is given by

$$\delta\rho(\mathbf{q}, \omega) = \frac{i}{2\pi} \sum_{\mathbf{k}} g(\mathbf{k}, \mathbf{q}, \omega) \quad (9)$$

with

$$g(\mathbf{k}, \mathbf{q}, \omega) = \text{Tr} \delta\hat{G}(\mathbf{k}, \mathbf{k}', \omega) - \text{Tr} \delta\hat{G}^*(\mathbf{k}', \mathbf{k}, \omega), \quad (10)$$

where $\mathbf{k} - \mathbf{k}' = \mathbf{q}$. The real-space QPI can be obtained as

$$\delta\rho(\mathbf{r}_i, \omega) = \frac{1}{N} \sum_{\mathbf{k}} \delta\rho(\mathbf{q}, \omega) e^{i\mathbf{k} \cdot \mathbf{r}_i}. \quad (11)$$

In the following, intraorbital Coulomb interaction parameter (U) is taken as 1.07eV with $J = 0.25U$ to keep the total magnetic moment per site less than unity. Band filling n_e is fixed at 6.03 (3% electron doping). Self-consistently obtained orbital magnetizations are $m_{3z^2-x^2} = 0.086$, $m_{xz} = 0.095$,

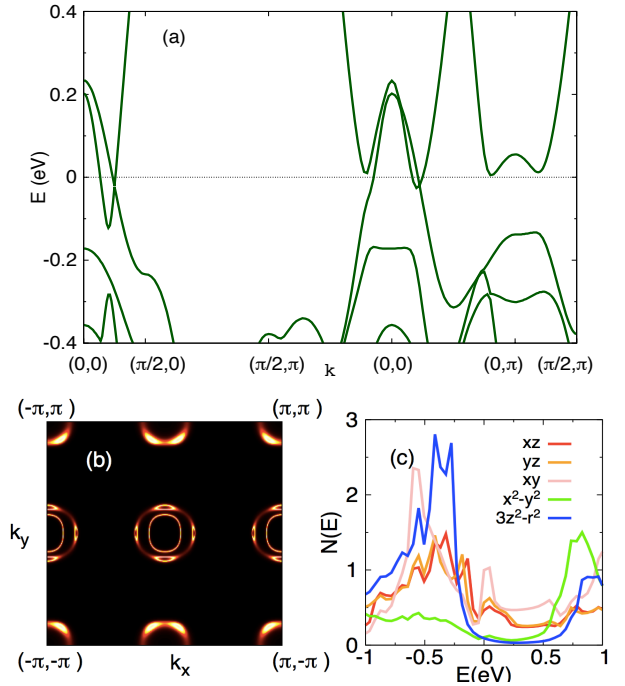


FIG. 1. (a) Electronic dispersion along the high-symmetry directions, (b) Reconstructed Fermi surfaces consisting of several pockets near and around Γ as well as around $(\pi, 0)$, and (c) orbital-resolved density of states in the $(\pi, 0)$ -SDW state.

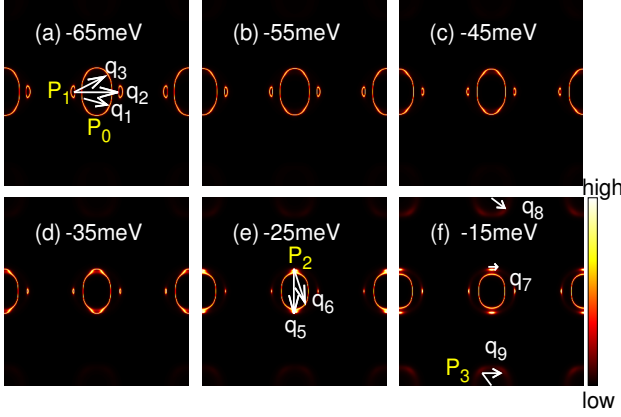


FIG. 2. Constant energy maps of the spectral functions $\mathcal{A}(\mathbf{k}, \omega)$ in the unfolded Brillouin zone from -65meV (top left) to -15meV (bottom right) in step of 10meV . The arrows represent scattering wavevectors in the SDW state. Note that \mathbf{q}_4 , \mathbf{q}_7 , and \mathbf{q}_{10} are not shown, which are the intrapocket scattering vectors for the tiny CCEs P_1 , P_2 , and for the subpockets in CCE P_3 , respectively.

$m_{yz} = 0.142$, $m_{xy} = 0.186$, and $m_{x^2-y^2} = 0.048$. Orbital charge densities are $n_{3x^2-x^2} = 1.469$, $n_{xz} = 1.208$, $n_{yz} = 1.182$, $n_{xy} = 1.014$, and $n_{x^2-y^2} = 1.158$. Strength of the impurity potential V_{imp} is set to be 200meV . Varying strength will change the intensity while the basic structure of the QPI is expected to remain the same. A mesh size of 300×300 in the momentum space is used for all the calculations.

III. RESULTS

Fig.1(a) and (b) show the electronic dispersion and the Fermi surface (FS) in the SDW state. The FS consists of an ellipse-like hole pocket around Γ , with major axis in the $(0, 1)$ direction, and tiny electron pockets situated at $\approx (\pm\pi/4, 0)$ and $(0, \pm\pi/4)$ but outstretched along $(0, 1)$ and $(1, 0)$ directions, respectively. Interestingly, similar pockets although larger in size have been reported by the ARPES experiments^{25,26}. In addition, there are electron pockets around $(0, \pm\pi)$. Some of the above characteristics of FSs lead to significant anisotropy in the QPI. Fig.1(c) shows that the d_{xy} , d_{yz} , and d_{zx} orbitals dominate at the Fermi level.

In order to understand the QPIs, it will be useful to look at the CCEs of the spectral functions, which are shown in Fig.2(a)-(f) as a function of energy with step of 10meV upto -15meV starting from -65meV . Near -65meV , CCEs consists of an ellipse-like pocket P_0 around $(0, 0)$ and two tiny pockets P_1 along $k_y = 0$ mapped onto each other by 180° rotation owing to the C_2 symmetry. Thus, there are four sets of scattering vectors - intrapocket scattering vectors \mathbf{q}_1 due to P_0 , interpocket scattering vectors \mathbf{q}_2 connecting the pockets of P_1 , interpocket scattering vectors \mathbf{q}_3 connecting P_0 and P_1 and intrapocket scattering vectors \mathbf{q}_4 (not shown in Fig.3(a)) due to P_1 . Corresponding QPI pattern is expected to have a two-dimensional nature because of a near cancellation of

two opposite tendencies in which scattering vectors \mathbf{q}_1 tries to create a one-dimensional pattern along the $(0, 1)$ direction while \mathbf{q}_2 and \mathbf{q}_3 do the same along the $(1, 0)$ direction. On the contrary, pattern consists of two parallel peak structures running along $q_x = \text{const}$ and passing through $q_x \approx (\pm\pi/4, 0)$ (Fig.3(a)).

In addition, there are small elliptical pockets located near $q_x \approx (\pm\pi/2, 0)$. Here, it is important to note that only those scattering vectors are important, which connect parts of the CCEs having same dominating orbitals because only intra-orbital scattering has been incorporated owing to the symmetry consideration¹³.

An important change in the QPI patterns occurs upon increasing the energy as shown in Fig.3(d). This happens primarily because of the appearance of a new set of CCEs in the form of tiny pockets P_2 , which emerge out of the elliptical pocket P_0 . Since P_2 is in the proximity of band extrema, pattern generated corresponding to the scattering vectors connecting these pockets should dominate the overall QPI pattern because of a larger phase space available for the scattering processes. Therefore, the balance maintained by the two opposite tendencies described above is perturbed now. This results into a highly anisotropic QPIs (Fig.3(d)) dominated by wavevectors \mathbf{q}_5 , \mathbf{q}_6 and \mathbf{q}_7 (Fig.3(c)). \mathbf{q}_5 and \mathbf{q}_7 are the set of interpocket and intrapocket scattering vectors for P_2 pockets, respectively, whereas \mathbf{q}_6 is another set of interpocket scattering vectors connecting P_0 and P_2 .

On increasing energy further, an additional set of CCEs appear near $(0, \pm\pi)$ as seen Fig.2(f), which may also contains very small subpockets (Fig.1(b)). As these are in the vicinity of local band extrema and parallel to the $k_y = 0$, two-dimensional characteristics is imparted to the QPIs as noticed in Fig.3(f). Dominating QPI wavevectors are due to the inter subpocket scattering vectors \mathbf{q}_8 and \mathbf{q}_9 as well as due to intra subpocket scattering vectors \mathbf{q}_{10} not shown (Fig.1(b)).

Several aspects of the QPI obtained here compare well with those of SI-STM measurements carried out for

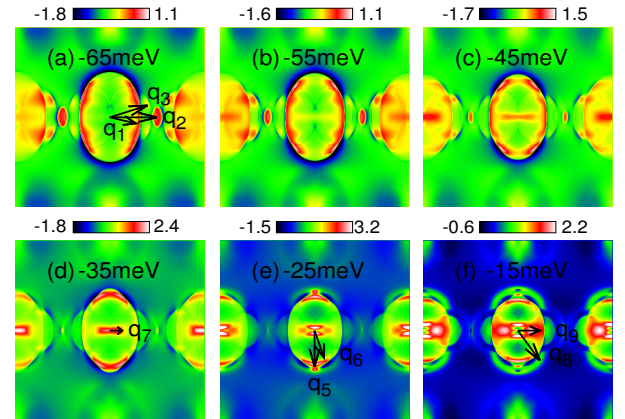


FIG. 3. QPI maps in the unfolded Brillouin zone for different energies ω upto -65meV (top left) to -15meV (bottom right) in steps of 10meV . The arrows denote the QPI wavevectors in the SDW state.

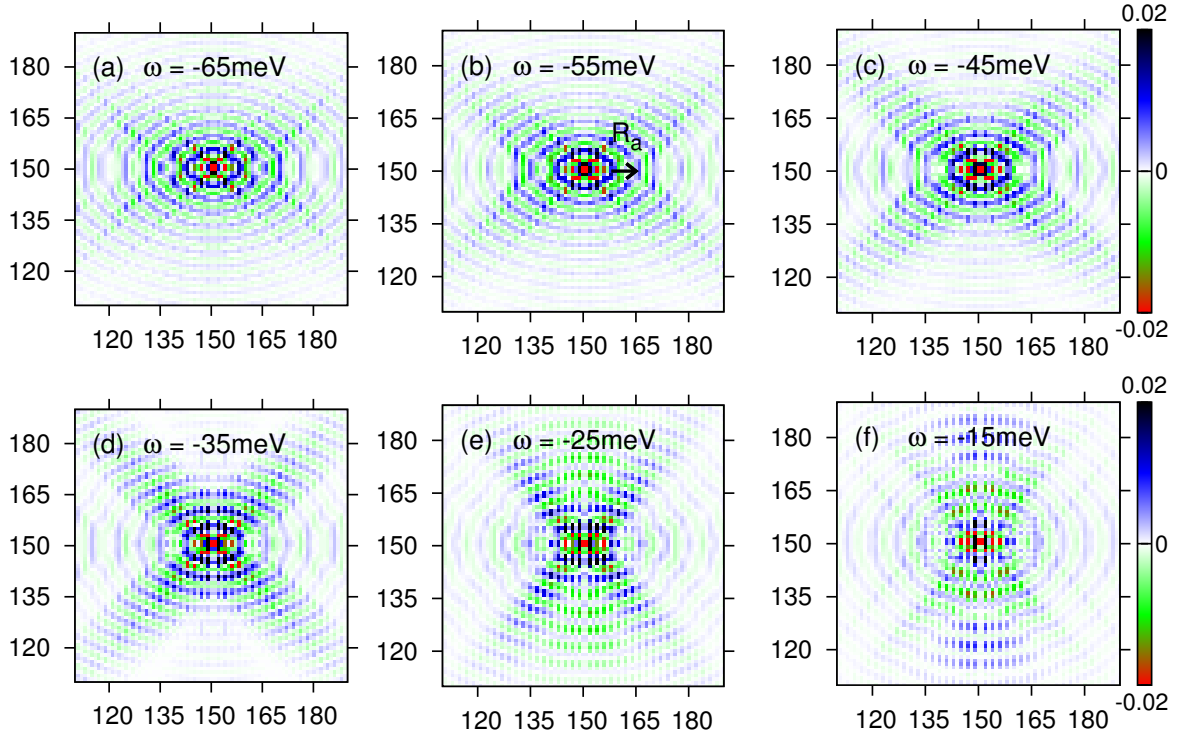


FIG. 4. Real-space QPIs for the set of parameters as in Fig.3. LDOS modulation along the antiferromagnetic direction (x -axis) with the wavelength $R_x \approx 8a_{\text{Fe-Fe}}$. Although the period of modulation along the antiferromagnetic direction remains almost unchanged, the strong modulation direction is sensitive to the quasiparticle energy.

$\text{Ca}(\text{Fe}_{1-x}\text{Co}_x)_2\text{As}_2$. For $\omega = -35\text{meV}$, a central peak structure runs along $q_x = 0$ and consists of three main peaks which themselves are made of multiple peaks either coinciding or placed very closely: one at $(0, 0)$, and other two placed equidistant from it. Additionally, there are parallel running satellite peak structures situated at $\approx (\pm\pi/4, 0)$, which are part of an elliptical QPI patterns. The quasi-one dimensional nature of the pattern is found in a wide energy window. These features are in agreement with the STM measurements. We also note that they very sensitive to energy as evident from Fig.3(e), when they become very weak for $\omega = -15\text{meV}$ on increasing the quasiparticle energy further. Features of the CCEs especially the existence of pockets along $k_x = 0$,

which play a crucial role in imparting the quasi-one dimensionality to the main peak structure, have also been noticed in the ARPES measurements. We have also examined the role of an orbital splitting term in the Hamiltonian, which is found to bring in only minor deviations because of a relatively large sized P_1 and also due to the suppression of pockets P_2 . Thus, it is the significant band reconstruction in the SDW state which is responsible for the experimentally observed anisotropy in the QPI.

Fig.4 shows corresponding real-space QPI pattern. The wavelength of LDOS modulation along x (antiferromagnetic direction) is $R_x \sim 8a_{\text{Fe-Fe}}$ for all energy values considered here though modulation may be weak or strong depending on the energy. A strong modulation along x is seen for energies $\omega = -65\text{meV}$ and -55meV , with parallel running peak structures along $q_x = \text{const}$ and passing through $q_x = 2\pi/R_x \approx (\pm\pi/4, 0)$ in qualitative agreement with the impurity induced electronic structure observed by the SI-STM experiments. However, it becomes stronger along $x \approx y$ upon increasing the energy and corresponds to a strong modulation of DOS in the momentum space along a direction tilted away from $q_x = \text{const}$.

IV. DISCUSSION

A. Physical mechanism

Our study highlights the role of redistributed orbital weight along the CCEs. In the unordered state, the hole pock-

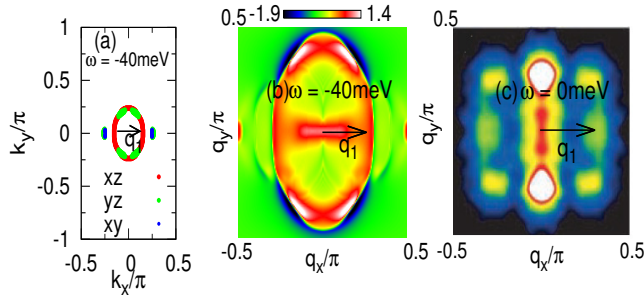


FIG. 5. (a) CCEs for $\omega = -40\text{meV}$ with dominant orbital character in the SDW state and (b) corresponding momentum-space QPI patterns. (c) QPI patterns observed in 3% electron-doped CaFe_2As_2 for $\omega = 0\text{meV}$ by the STM.¹⁶

ets around Γ have predominantly d_{xz} and d_{yz} character distributed in way to respect the four-fold rotational symmetry. On the contrary, the CCE pocket around Γ in the SDW state is dominated by the d_{xz} orbital. For $\omega = -65\text{meV}$, the scattering vectors connecting the regions near the vertices along the minor axis of elliptical pocket leads to the most intense region in the QPI. This happens primarily because of two reasons. First, a larger phase space is available when compared with the case of scattering vectors connecting the vertices along the major axis. Secondly, only intraorbital scattering processes are taken into account. On increasing energy, a small d_{yz} rich region (Fig.5(a)) appears along the elliptical CCE as a new band crosses the quasiparticle energy. Because of the new band's extrema and associated large spectral weight, QPI pattern due to the scattering vectors connecting d_{yz} rich regions prevails over the others (Fig.5(b)). Consequently, the most intense region moves towards the vertices along the major axis (Fig.3(b)-(d)) a features present also in the STM results (Fig.5(c)).

In this work, the focus was on the LDOS modulation. Another important issue is the modulation in the local magnetization induced by in the vicinity of the impurity. This has been addressed in a recent work within a self-consistent approach for single non-magnetic impurity²⁰. The study found that the impurity induces magnetic nanostructures with checkerboard-type order inside, extended along the antiferromagnetic direction with a significant LDOS modulation at the ends. Our result on the LDOS modulation in real-space is also consistent with this study.

B. Comparison with earlier work

Anisotropy in the QPI patterns of the SDW state is not unexpected because of the breaking of four-fold rotational symmetry. However, the details of the patterns depend on the electronic structure. A plausible description of the QPI patterns restrict the modeling of the electronic structure. The failure of almost all the earlier work in reproducing the nearly parallel running satellite peak structures along $q_x \approx \pm\pi/4$ highlights the limitation of the electronic structure used. In our work, these structures result from the elliptical CCE around $(0,0)$ with a major role played by the scattering vectors lying nearly parallel to the minor axis of length $\sim \pi/4$. Thus, we believe that the Fermi pocket around Γ , the existence of which has also been suggested by the ARPES measurements, is likely to

be elliptical in shape.

C. Unresolved issues

For 3% doping on the parent state the $8a_{\text{Fe-Fe}} \times 8a_{\text{Fe-Fe}}$ nanostructures would contain more than one impurity atom on the average. Therefore, the interference between scattering events from multiple impurities could be important for the measured QPI patterns. The present t-matrix approach unfortunately does not access these effects. Recently, a framework to study QPI in the presence of interacting multiple impurities has been discussed³¹. However, in many instances, single impurity treatment has yielded QPI patterns which successfully describe the qualitative features of STM measurements. The LDOS modulation obtained in this work with the periodicity $\sim 8a_{\text{Fe-Fe}}$ is another such example.

LDOS modulation with the experimentally observed periodicity is reproduced successfully in our results along the antiferromagnetic direction, and is robust against any change in the quasiparticle energy. However, the strongly modulated direction exhibits sensitivity to the quasiparticle energy, which is due to the fast change in the CCEs. In the experiments, however, the strongly modulated direction is robustly along the antiferromagnetic direction despite the change in energy. This may indicate that CCEs change comparatively slowly in the real systems as a function of energy.

V. CONCLUSIONS

We have investigated the quasiparticle interference pattern in the $(\pi, 0)$ -SDW state using a five-orbital tight-binding model of electron-doped iron pnictides. With a realistic reconstructed bandstructure, which includes an ellipse-like constant energy contour around $(0, 0)$ and additional nearby smaller pockets, we find highly anisotropic QPI patterns. Because the scattering vectors oriented along the minor axis of the elliptical CCE (of length $\pi/4$) connects d_{xz} rich segments, QPI peak structures are obtained at $(\pm\pi/4, 0)$, running parallel to the q_y axis. The corresponding real-space pattern consists of LDOS modulation along the antiferromagnetic direction with periodicity $\sim 8a_{\text{Fe-Fe}}$. Both the features are in agreement with STM results for the doped iron pnictides.

We acknowledge use of the HPC Clusters at HRI.

¹ M. Yi, D. Lu, J.-H. Chu, J. G. Analytis, A. P. Sorini, A. F. Kemper, B. Moritz, S.-K. Mo, R. G. Moore, M. Hashimoto, W.-S. Lee, Z. Hussain, T. P. Devereaux, I. R. Fisher, and Z.-X. Shen, Proc. Natl. Acad. Sci. **108**, 6878 (2011).

² T. Shimojima, K. Ishizaka, Y. Ishida, N. Katayama, K. Ohgushi, T. Kiss, M. Okawa, T. Togashi, X.-Y. Wang, C.-T. Chen, S. Watanabe, R. Kadota, T. Oguchi, A. Chainani, and S. Shin, Phys. Rev. Lett. **104**, 057002 (2010).

³ M. Fu, D. A. Torchetti, T. Imai, F. L. Ning, J.-Q. Yan, and A. S.

Sefat, Phys. Rev. Lett., **109**, 247001 (2012).

⁴ J.-H. Chu, J.-H. Chu, J. G. Analytis, K. De Greve, P. L. McMahon, Z. Islam, Y. Yamamoto, and I. R. Fisher, Science **329**, 824 (2010).

⁵ M. A. Tanatar, E. C. Blomberg, A. Kreyssig, M. G. Kim, N. Ni, A. Thaler, S. L. Bud'ko, P. C. Canfield, A. I. Goldman, I. I. Mazin, and R. Prozorov, Phys. Rev. B **81**, 184508 (2010).

⁶ E. C. Blomberg, M. A. Tanatar, R. M. Fernandes, I. I. Mazin, B. Shen, H.-H. Wen, M. D. Johannes, J. Schmalian, and R. Prozorov, Nat. Commun. **4**, 1914 (2013).

- ⁷ S. Nandi, M. G. Kim, A. Kreyssig, R. M. Fernandes, D. K. Pratt, A. Thaler, N. Ni, S. L. Budko, P. C. Canfield, J. Schmalian, R. J. McQueeney, and A. I. Goldman, *Phys. Rev. Lett.*, **104**, 057006 (2010).
- ⁸ M. Rotter, M. Tegel, D. Johrendt, I. Schellenberg, W. Hermes, and R. Pöttgen, *Phys. Rev. B*, **78**, 020503R (2008).
- ⁹ M. Nakajima, T. Liang, S. Ishida, Y. Tomioka, K. Kihou, C. H. Lee, A. Iyo, H. Eisaki, T. Kakeshita, T. Ito, and S. Uchida, *Proc. Natl. Acad. Sci. U.S.A.* **108**, 12238 (2011).
- ¹⁰ L. Capriotti, D. J. Scalapino, and R. D. Sedgewick, *Phys. Rev. B* **68**, 014508 (2003).
- ¹¹ S. Sykora and P. Coleman, *Phys. Rev. B* **84**, 054501 (2011).
- ¹² A. Kreisel, Peayush Choubey, T. Berlijn, W. Ku, B. M. Andersen, and P. J. Hirschfeld, *Phys. Rev. Lett.* **114**, 217002 (2015).
- ¹³ Y.-Y. Zhang, C. Fang, X. Zhou, K. Seo, W.-F. Tsai, B. A. Bernevig, and J. Hu, *Phys. Rev. B* **80**, 094528 (2009).
- ¹⁴ Y. Yamakawa and H. Kontani *Phys. Rev. B* **92**, 045124 (2015).
- ¹⁵ P. J. Hirschfeld, D. Altenfeld, I. Eremin, and I. I. Mazin *Phys. Rev. B* **92**, 184513 (2015).
- ¹⁶ T.-M. Chuang, M. P. Allan, J. Lee, Y. Xie, N. Ni, S. L. Budko, G. S. Boebinger, P. C. Canfield, and J. C. Davis, *Science* **327**, 181 (2010).
- ¹⁷ E. P. Rosenthal, E. F. Andrade, C. J. Arguello, R. M. Fernandes, L. Y. Xing, X. C. Wang, C. Q. Jin, A. J. Millis and A. N. Pasupathy, *Nature Physics* **10**, 225 (2014).
- ¹⁸ X. Zhou, C. Ye, P. Cai, X. Wang, X. Chen, and Y. Wang, *Phys. Rev. Lett.* **106**, 087001 (2011).
- ¹⁹ M. P. Allan, T.-M. Chuang, F. Massee, Yang Xie, Ni Ni, S. L. Budko, G. S. Boebinger, Q. Wang, D. S. Dessau, P. C. Canfield, M. S. Golden, and J. C. Davis, *Nature Physics* **9**, 220 (2013).
- ²⁰ M. N. Gastiasoro, P. J. Hirschfeld, and B. M. Andersen *Phys. Rev. B* **89**, 100502 (2014).
- ²¹ J. Knolle, I. Eremin, A. Akbari, and R. Moessner, *Phys. Rev. Lett.* **104**, 257001 (2010).
- ²² S. Graser, T. A. Maier, P. J. Hirschfeld, and D. J. Scalapino, *New J. Phys.* **11**, 025016 (2009).
- ²³ N. Plonka, A. F. Kemper, S. Graser, A. P. Kampf, and T. P. Devereaux, *Phys. Rev. B* **88**, 174518 (2013).
- ²⁴ H.-Y. Zhang and J.-X. Li, *Phys. Rev. B* **94**, 075153 (2016).
- ²⁵ M. Yi, D. H. Lu, J. G. Analytis, J.-H. Chu, S.-K. Mo, R.-H. He, M. Hashimoto, R. G. Moore, I. I. Mazin, D. J. Singh, Z. Hussain, I. R. Fisher, and Z.-X. Shen, *Phys. Rev. B* **80**, 174510 (2009).
- ²⁶ Q. Wang, Z. Sun, E. Rotenberg, F. Ronning, E. D. Bauer, H. Lin, R. S. Markiewicz, M. Lindroos, B. Barbiellini, A. Bansil, and D. S. Dessau, *arXiv:1009.0271*
- ²⁷ I. I. Mazin, S. A. J. Kimber, and D. N. Argyriou, *Phys. Rev. B* **84**, 054501 (2011).
- ²⁸ H. Ikeda, R. Arita, and J. Kunes, *Phys. Rev. B* **81**, 054502 (2010).
- ²⁹ S. Ghosh and A. Singh, *New J. Phys.* **17**, 063009 (2015).
- ³⁰ D. K. Singh and T. Takimoto, *J. Phys. Soc. Jpn.* **85**, 044703 (2016).
- ³¹ A. K. Mitchell, P. G. Derry, and D. E. Logan, *Phys. Rev. B* **91**, 235127 (2015).